Large-format fabrication by two-photon polymerization in SU-8

Yihong Liu · David D. Nolte · Laura J. Pyrak-Nolte

Abstract Microporous structures are central to many fields of science and engineering, but many of these systems are complex with little or no symmetry and are difficult to fabricate. We applied two-photon polymerization (2PP) and femtosecond laser direct-writing techniques to fabricate broad-area large-format 3D microporous structures (450 μm × 450 μm × 40 μm) in the epoxy-based photoresist SU-8. The appropriate exposure was determined by controlling average pulse energies and stage speeds to generate the exposure curves. Mechanical distortion exhibited in suspended walls fabricated by 2PP laser writing was studied by controlling wall lengths and widths. A simple thermal-expansion model is presented to explain the distortion caused by axial loadings of the walls.

1 Introduction

Two-photon polymerization (2PP) was first reported by Pao and Rentzepis in 1965 [1]. In the late 1980s 2PP attracted attention in the field of optical recording. In 1989, Parthenopoulos and Rentzepis reported a novel optical memory device based on two-photon writing and reading in photochromic materials [2], and in 1991 the first high-density ($>10^{12}$ bits/cm^3) optical storage in a multi-layered format was achieved by two-photon excitation in a photopolymer [3]. Subsequently, many research fields have made progress using 2PP, such as microdevice and photonic crystal fabrication [4–6]. In 1997, a spiral structure, the first three-dimensional (3D) microstructure fabricated by 2PP, was reported. The width of the spiral wire was 1.3 μm [7]. Complex 3D microstructures, devices, and optics have been fabricated by 2PP, such as a microgear-wheel [8], microrotor [9], microchain [10], microlens [11, 12], and optical circuits [13, 14]. The voxel diameter was pushed to 120 nm, much lower than the diffraction limit, and a microbull was presented in 2001 [15]. The smallest feature reported to date is approximately 60 nm, achieved with 520 nm femtosecond pulses [16, 17]. On the other hand, fabricating micro/nanostructures in a large area is a novel field. 3D periodic metallic microstructures over an area of 170×125 μm^2 were fabricated by combining 2PP with microlens arrays [18]. But write-time is a problem when fabricating non-periodic patterns, e.g. a raised-relief 450×260 μm^2 world map required about 9 h for layer-by-layer accumulation [19].

Microporous structures are central to many fields of science and engineering, ranging from biological tissue [20] and fluidic filters [21] to porous aquifers [22]. Most of these systems are complex with little or no symmetry. Although multilayer microstructures have been fabricated using broad-illumination photolithography, arbitrary 3D microfluidic structures are too complex to be made with linear exposure. Two-beam interference can achieve periodic structure fabrication, such as photonic crystals [23]. Two-photon polymerization (2PP), on the other hand, would be a means to generate arbitrarily complex microfluidic systems. Furthermore, 2PP has been shown to push microstructure dimensions beyond the diffraction limit and provides the advantage of fabricating submicron structures [15].

Y. Liu (✉) · D.D. Nolte · L.J. Pyrak-Nolte
Department of Physics, Purdue University, 525 Northwestern Avenue, West Lafayette, IN 47907, USA
e-mail: liu84@purdue.edu
Fax: +1-765-4940706

L.J. Pyrak-Nolte
Department of Earth and Atmospheric Sciences, Purdue University, 550 Stadium Mall Dr, West Lafayette, IN 47907, USA

In this paper, we demonstrate a 2PP system with the capability to fabricate arbitrary 3D microfluidic structures, including inlet and outlet ports for fluid flow, and we employed the system to fabricate two types of large-scale 3D micromodels (450 μm × 450 μm × 40 μm) to simulate microporous structures. The system consists of a low-power femtosecond laser that exposes photoresist (SU-8) on an XYZ translation stage. SU-8 is an epoxy-based negative photoresist sensitive to near-UV wavelengths under 400 nm.

2 Two-photon polymerization in SU-8

We used the negative photoresist Nano SU-8 (Microchem Co.) for our microfabrication. This type of photoresist is widely used in applications of microelectro mechanical systems (MEMS). SU-8 epoxy is a multifunctional glycidyl ether derivative of bisphenol-A novolac from Shell Commercial's EPON SU-8 resin [24]. There are 8 epoxy groups in each molecule. This resist has high cross-linking performace, allows a high aspect ratio, improves side-wall straightness, and has better chemical thermal resistance [25]. Furthermore, because SU-8 has a low molecular weight around 7000, it dissolves in a variety of organic solvents, resulting in less developer-induced pattern swelling and thus high resolution [24, 26]. For example, a 190 nm diameter post was reported by Lee et al. in 2004 [27]. In addition, the absorption in the near-UV spectrum is very low so that light can penetrate thick photoresist layers and thus fabricate thick films [28]. A 500-μm thick layer with an aspect ratio of 50:1 was reported by Teh et al. in 2005 [29].

SU-8 epoxy is dissolved in gamma butyrolactone (GBL) to adjust the viscosity and achieve different film thickness ranges. Less GBL and more SU-8 results in higher viscosity and thicker film range, e.g. SU-8/GBL = 7:3, thickness = 30–200 μm; SU-8/GBL = 6:4, thickness = 5–25 μm; with spin speeds from 1000–4000 rpm [30]. The third component is a photoinitiator, triaryl sulfonium salt in propylene carbonate solvent. Under UV exposure, this salt generates catalyzed acid, which helps open the ring and gain much higher cross-linking efficiency. During the subsequent baking, the photogenerated acid diffuses in the photoresist and catalyzes the cross linking. Because the uncrosslinked resist has low molecular weight, the unexposed resist can be removed by a nonpolar solvent, forming a negative image. The difference of the solubility between the exposed and unexposed resists determines the pattern resolution [26].

SU-8 is optimized for near-UV (350–400 nm) exposure, insensitive above 400 nm but highly absorptive below 350 nm. Therefore, to reduce negative sidewall effect and gain high-quality microstructures, a band or long-pass filter is used to cut off the energy below 350 nm when doing UV exposure [31]. The optimal exposure dosage depends on the photoresist thickness, and a thicker resist layer requires a higher exposure dosage [32]. The maximum and minimum exposure dosages recommended in the company's data sheet are 350 and 200 mJ/cm^2 for a 40-μm thick layer [31]. 2PP has been applied to UV-sensitive photoresists, such as SU-8, SCR-500, and Nopcocure 800 resin [7, 33], by focusing a near-IR laser pulse through an objective lens into the photoresist. Because of the high photon flux at the focus, the photo initiators absorb two low-energy photons simultaneously and complete the acid-generation reaction sensitive to the UV spectrum. The resist is transparent to near-IR radiation and only the volume around the focus has a high photon flux so that the photoresist can be exposed locally in a small volume. The polymerization rate depends quadratically on the photon flux density [34].

3 Experimental apparatus and procedures

3.1 Optical system

The optical setup for the two-photon polymerization (2PP) system to create three-dimensional micromodels is shown in Fig. 1. The light source is a femtosecond oscillator (Clark-MXR NJA-4) pumped by a continuous-wave diode-pumped solid-state laser (Coherent Verdi-5) with high-power stability ±1% and low noise <0.03% rms. The pump laser power is 4 W with a wavelength of 532 nm. The 2.25 mm diameter beam is introduced into the tunable mode-locked Ti:Sapphire laser through beam steering optics to pump the Ti:Sapphire laser crystal, and a prism pair is used for dispersion compensation. The nominal femtosecond pulse duration is 100 fs, the repetition rate is 100 MHz, and the pulse energy is up to 3.5 nJ/pulse. The center wavelength is adjusted to 790 nm because the photoresist SU-8 is optimized for 350 nm ∼ 400 nm (near UV) exposure for single-photon absorption, i.e. 700 nm ∼ 800 nm for two-photon absorption. The laser operates most effectively at a wavelength of 800 nm. The full-width half maximum of the frequency spectrum is 36 nm.

Figure 1 shows the 2PP experimental setup used to create three-dimensional micromodels. The femtosecond pulses are focused through a 20×, 0.75 NA objective lens into the photoresist-coated cover slip that sits on a XYZ motion-controlled stage. The x and y stages have a minimum increment of 50 nm (Newport Actuator LTA-HL) and 200 nm for the z direction stage (Newport CMA-12CCCL). The motion of the stages is computer-controlled. The main optical path includes a neutral density filter that attenuates the average beam power (optical density gradient 0.05 ∼ 1), a shutter that sets the exposure time (minimum exposure time 2 ms, Uniblitz LS6T2), and a beam expander composed of a concave lens ($f = -50$ mm) with a convex lens ($f = 150$ mm)

Fig. 1 The experimental setup for two-photon polymerization (2PP) to create three-dimensional microfluidic structures. The 100 MHz, 790 nm central-wavelength mode-locked femtosecond laser pulses are focused through a $20\times$, 0.75 NA, objective lens into the SU-8 sample on a XYZ motion stage. The inset graph shows the signal output of the photodetector used to adjust the stage level
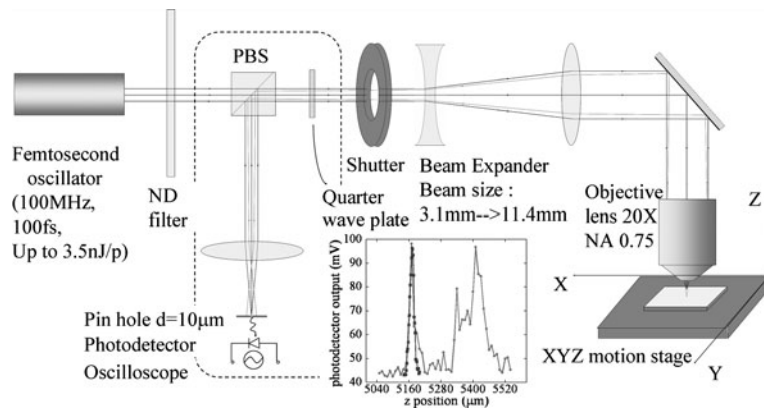
to expand the beam diameter. The average power and exposure time determine the exposed volume. A small focal spot radius produced by the expanded beam yields a small height-to-width ratio of the exposure shape. In a branch path, we constructed a confocal system to locate the photoresist surface and to determine the z coordinates of the exposure position. Based on the system parameters, the confocal pinhole diameter is half of the Airy unit, and is approximately 10 μm. The pinhole is located behind a convex lens with a focal length of 50 mm and immediately in front of the photodetector (Thorlabs DET110). A quarter-wave plate and a polarized beam splitter are also employed to direct the reflected light to the photodetector to collect and to prevent the reflected light from returning to the laser cavity.

Before exposing a sample, the level of the system is checked to ensure that the focal depth is at the same Z coordinate for different X and Y coordinates. First, the Z coordinates of the photoresist surface at the four corners of the sample are determined by using the confocal system. Second, the stage is adjusted so all four z coordinates are the same. For each position, only the stage in the z direction is moved with a step length of 10 μm for a total of 50 steps. At each point, the output of the photodetector is recorded. The photoresist surface is determined from a graph of the detector signal plotted against the vertical position z shown in Fig. 2. The procedure is repeated with 2 μm/step and 30 steps to refine the location of the Z coordinate. By this procedure, we adjusted the 4 corners to the same level and ensured the sample surface was perpendicular to the laser direction (Z direction). In addition, the peak position indicates the Z coordinate of the air—SU-8 surface. Considering the SU-8 layer thickness, we found the Z coordinate of the SU-8—glass interface, and thus located the exposure volume along the Z-axis.

3.2 Photoresist

The samples are made of SU-8 photoresist spin-coated on a substrate cover glass. The cover glass is 18 mm × 18 mm and approximately 250 μm thick. Before spin-coating, the cover glass is cleaned in DI water, acetone, and isopropyl alcohol in an ultrasonic cleaner (Branson 1510) for 5 min for each step, and dried with nitrogen. About 0.1 ml SU-8 50 (Microchem) is applied on the center of the cover glass and spin-coated at 3000 rpm to produce a 40-μm thick layer. Before soft baking, the sample is placed on a flat surface at room temperature for about one hour to reduce the edge effects of spinning. The sample is then baked in an oven at 65°C and 95°C for 15 min and 30 min, respectively, to evaporate the solvent and densify the film. The sample is gradually cooled down to room temperature to avoid introducing stress.

The sample is exposed in two steps: (1) with the femtosecond laser to expose the desired structure in the center of the sample; and (2) with a UV lamp to expose inlet and outlet regions for fluid flow experiments. For (1), the sample is placed on the XYZ motion stage and the stage is moved to direct-write the desired pattern into the photoresist layer on the sample. The exposure position and speed are set by computer. Following the two-photon exposure, a UV lamp is used to expose the 3 mm × 3 mm inlet and outlet ports. Between the ports, there is a 900 μm × 700 μm unexposed area left for the pattern. For two-photon exposure the Ti:Sapphire laser is adjusted to a center wavelength at 790 nm.

After exposure, the photoresist is baked at 65°C and then 95°C for 10 min and 15 min, respectively to cross-link the SU-8. The sample is cooled slowly to room temperature to avoid introducing stress. The sample is developed in a commercial developer (Microchem) for 6 min, rinsed in isopropyl alcohol, and placed on a flat surface to dry. We do not hard-bake the sample because the sample is strong enough for flow studies. For flow testing, two holes with diameters of 0.0225 inches are drilled in the inlet and outlet ports on the substrate before development, and then the sample is sealed with a cover glass spin-coated a thin layer of SU-8. The microfluidic sample applications are described elsewhere [35–38]. In this paper we focus on broad-area fabrication.
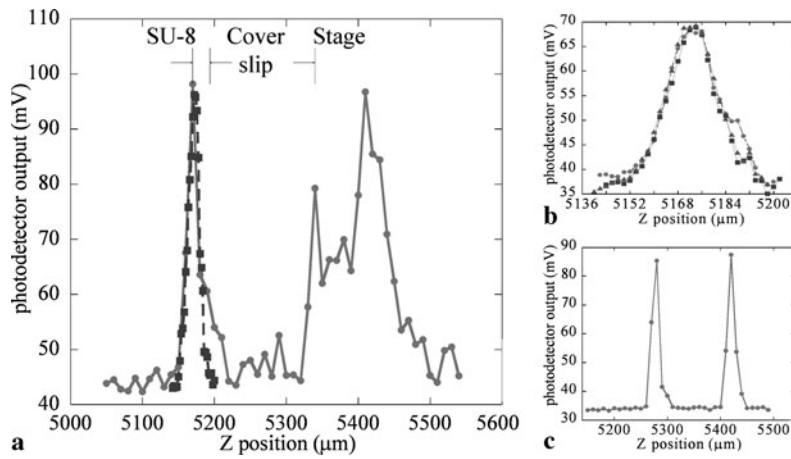
Fig. 2 Photodetector outputs of the confocal system. **a** The 50-step scan over a range of 500 μm includes the top and bottom surfaces of the sample. The peak overlapped with the *dash curve* shows the air–SU-8 surface. The peaks are the reflection from the air–glass interface and the scatter from the stage; **b** higher-resolution scans for the *dash curve* in (**a**). The curves indicated by different symbols were scanned at different corners of the sample; **c** a scan of a cover glass (no SU-8 layer, no stage scattering). The two peaks indicate the air–glass and glass–air surfaces of the cover glass

3.3 Characterization

Optical and scanning electron micrographs are the primary characterization methods used for the calibration and study of the structures. The optical images were acquired with a Leica DMRX microscope and the SEM images were acquired with a JEOL JSM 35CF scanning electron microscope. Optical micrographs were taken through the reflection channel of the microscope with a charged coupled device (CCD) camera (Qimage Retiga 4000R Fast), averaged 16 times, and saved as an 8-bit tif-file. The image resolution is 0.71 μm/pixel under a magnification of $20\times$. Based on images taken at this resolution, the wall shape is extracted from the raw image and used to study the mechanical instability of the walls.

The SEM micrographs were acquired with an accelerating voltage of 25 kV and a filament gun current of 95 μA. Before taking SEM images, gold/palladium was sputtered onto the sample surface for 1 min, about 3 nm thick, in a Hummer 6.2 sputtering system. Magnification and length scale bars are shown in each image. The SEM images used for wall calibration were all taken at a magnification of $1500\times$, and the corresponding resolution is 74 nm.

4 Calibration of two-photon polymerization exposure

4.1 Exposure model

We used 2PP to fabricate 3D microporous structures. The two-photon transition rate is defined by

$$R_{\text{if}}^{(2)} = \left| \sum_{\text{m}} \frac{\mu_{\text{fm}}\mu_{\text{mi}}E^2}{\hbar^2(\omega_{\text{mi}} - \omega)} \right|^2 2\pi\rho_{\text{f}}(\omega_{\text{fi}} = 2\omega) \tag{1}$$

where the subscripts i, m, and f, represent initial, middle, and final states, respectively. $\rho_{\text{f}}(\omega_{\text{fi}} = 2\omega)$ is the density of the final states excited by photons of energy $\hbar\omega$, Planck's constant $\hbar$ and the frequency ω. μ_{fi} is the transition dipole moment. The transition rate varies as $R \propto E^4 \propto I^2$ where I is the light intensity. Thus, the 2PP rate is proportional to the square of the intensity. The rate is also proportional to the duration that the photoresist is exposed by the femtosecond pulses. Therefore, the condition for 2PP is

$$I^2\beta\tau\upsilon t \geq F_{\text{th}} \tag{2}$$

where F_{th} is the 2PP threshold of SU-8, I is the peak intensity, β is a constant, τ is the pulse duration, υ is the repetition rate, and t is the exposure time. The intensity profile is assumed to be Gaussian

$$I(r, z) = I(z)e^{-2\left(\frac{r}{w(z)}\right)^2} \tag{3}$$

$$I(z) = \frac{2P}{\pi w(z)^2} \tag{4}$$

where $w(z)$ is the spot radius at the z plane, r is the radius in $x-y$ plane, and P is the average power. At the focal plane

$$I(r) = I_0 e^{-2\left(\frac{r}{w_0}\right)^2} \tag{5}$$

where w_0 is the $1/e^2$ focal spot radius and $I_0 = I(z = 0)$. Substituting the intensity in (2) by the Gaussian profile yields

$$d = w_0\sqrt{\ln\left(\frac{I_0^2 t}{C_{\text{th}}}\right)} \tag{6}$$

$$C_{\text{th}} = \frac{F_{\text{th}}}{\beta \tau \upsilon} \tag{7}$$

where d is the diameter of the exposure dose at the focal plane. Considering a Gaussian profile again, the height of the exposed region is

$$H = \frac{2z}{n} = \frac{2z_{\text{R}}}{n} \sqrt{\exp\left(\frac{1}{2}\left(\frac{d}{w_0}\right)^2\right) - 1} \tag{8}$$

$$z_{\text{R}} = \frac{\pi w_0^2}{\lambda} \tag{9}$$

where z_{R} is the Rayleigh range, λ is the wavelength, and $n = 1.7$ is the refractive index of SU-8. Because the stage speed is inversely proportional to the exposure time, combining (4) and (6), gives

$$w_{\text{wall}} = w_0 \sqrt{\ln\left(\frac{4P^2}{\pi^2 w_0^2 C'_{\text{th}} v}\right)} \tag{10}$$

$$C'_{\text{th}} = \frac{F'_{\text{th}}}{\beta \tau \upsilon} \tag{11}$$

where w_{wall} is the width of the wall, v is the stage speed, F'_{th} is the 2PP threshold of SU-8 in terms of exposure speed, and C'_{th} is a constant [27, 39, 40].

From (6), (8), and (10), the width and height of the exposed region is related to the light intensity, exposure time, and the focal spot radius. Smaller exposed volumes are obtained by lowering the intensity and shortening the exposure time. Larger focal spot radii produce low ratios of the height to width. We add a beam expander into the optical system to reduce the focal spot radius and the height-to-width ratio of the exposed region. Without the beam expander, the focal spot radius is 8 μm and the aspect ratio is approximately 27:1. Adding the beam expander reduces the focal spot radius to 4 μm and the height-to-width ratio to 10:1. To measure the focal spot radius, a sharp blade was translated across the focal plane and the power was measured and fit to an error function to acquire the focal spot radius w_0. The focal spot radii along the X- and Y-axis are calculated separately and the mean value is used in our study. We calculated the Rayleigh range from (9). In Table 1, we list parameters with and without the beam expander.

4.2 Calibration experiments

With the goal of fabricating microfluidic structures, we began by exposing posts and walls under different experimental conditions and fit the width using the theoretical model. Figures 3a and b show an example of exposed posts and walls. The posts or walls were exposed at different focal depths. If the focal depth is deep, the exposure volume is

Table 1 Optical system parameters

Focal spot radius w_0 (μm)	Rayleigh range z_{R} (μm)	Width (μm)	Height (μm)	Height-to-width ratio	Beam Expander
8	251	5.5	150	27	No
4	63	2	20	10	Yes

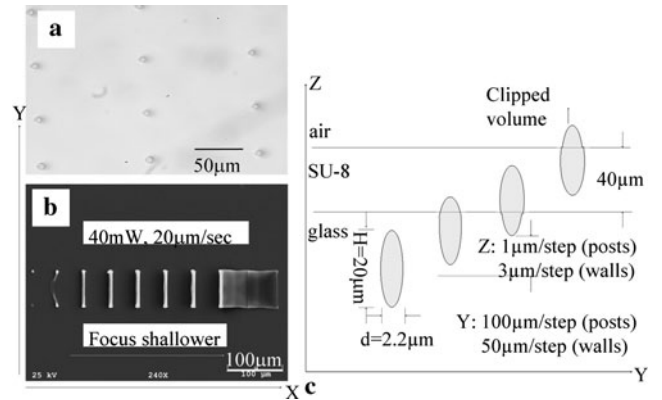**Fig. 3 a** Optical micrograph of posts at a magnification of 40× exposed with 300 mW and 50 ms. The focal depth becomes shallower from left to right in the X direction and remains the same in the Y direction; **b** an SEM image of straight walls for the wall-width measurement as a function of average power and exposure speed (average power 40 mW, speed 20 μm/s, magnification 240×, and wall length 80 μm). **c** The calibration experimental design in the axial section. The focal depth in the Z-axis becomes deeper from right to left in the Y-axis and remains the same in the X direction. The first exposure on the right has the shallowest focal depth and does not attach to the glass. The dimensions indicated on the first exposure on the left volume are the height and width of the exposed wall at 10 mW, 10 μm/s

completely buried in the glass, and no photoresist is exposed. On the other hand, if the focal depth is too shallow the posts or walls do not attach to the substrate, and no structure is left after the development. Thus, a focal depth must be chosen to ensure that the posts and walls attach to the substrate.

In our calibration experiments, we exposed posts and walls at different focal depths. The experimental approach is shown in Fig. 3c. We exposed wall by wall oriented in the Y direction and separated by 50 μm in the X direction. As the exposed position Y varied, the focal position in the Z direction was made deeper by 3 μm/step from right to left in Fig. 3c. As shown in Fig. 3b, the wall on the left is focused the deepest in the photoresist and is barely visible on the substrate. The first two walls on the right fell onto the substrate because the focal depths were too shallow for these two walls to remain attached to the cover glass after development. The focal depths of the posts were also changed in the same way, stepping in the X direction and held constant in the Y direction. The step sizes for the posts
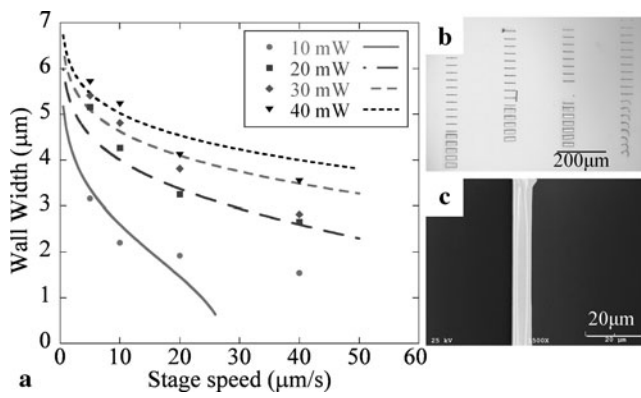
Fig. 4 **a** Wall widths under different average powers (10 mW, 20 mW, 30 mW, and 40 mW) as a function of stage speed (5 μm/s, 10 μm/s, 20 μm/s, and 40 μm/s), $w_0 = 4$ μm; **b** optical microscope image of walls exposed under 30 mW and speed from 5 μm/s to 40 μm/s from left to right, and the focal depth is deeper into the photoresist from the bottom to the top of the figure with 2 μm/step; **c** magnification 1.5k used for wall-width measurements and shown as data in (**a**)

Fig. 5 **a** Feature height under different average powers (10 mW, 20 mW, 30 mW, and 40 mW) as a function of stage speed (5 μm/s, 10 μm/s, 20 μm/s, and 40 μm/s), $w_0 = 4$ μm; **b** SEM image of walls exposed using 10 mW and 20 μm/s, magnification 240×. **c** Walls are under-exposed and not fully polymerized, using 10 mW and 40 μm/s, magnification 240×

were 100 μm/step along the X-axis and 50 μm/step along the Y-axis.

We studied the wall in terms of the average power and the stage speed using the experimental design described above. Figure 4a shows the wall widths under different average powers as a function of the stage speed. We exposed walls at an average power of 10 mW, 20 mW, 30 mW, and 40 mW, and for each power we used a stage speed of 5 μm/s, 10 μm/s, 20 μm/s, and 40 μm/s. Figure 4b shows an example of the exposed walls, at a power of 30 mW using 4 different speeds. The stage speed was increased from left to right, and the focus was decreased from top to bottom with a step of 2 μm per wall. As observed, some walls at the bottom of the image tipped over onto the substrate because of the shallow focal depth. Similar exposures were taken at the other three average powers.

We measured the widths of the walls from the SEM images at a magnification of 1500× (e.g. Fig. 4c) and fit the width with (10), as shown in Fig. 4a). The parameter in the fitting is $C'_{th} = 5.74 \pm 0.86 \times 10^{-3}$ mW^2 s/μm^5, which gives the threshold for direct writing a wall at $w_{wall} = 0$. According to (10), the exposure condition is

$$\frac{4P^2}{\pi^2 w_0^2 C'_{th} v} \geq 1 \qquad (12)$$

where P is the average power, v is the stage speed, and w_0 is the $1/e^2$ focal spot radius. Substituting in the value for C'_{th}, gives

$$\frac{P^2}{v} \geq 3.6 \ \frac{\text{mW}^2}{\text{μm/s}} \qquad (13)$$

If (13) is not satisfied, then the photoresist will be under-exposed and not fully polymerized. An example of an under-
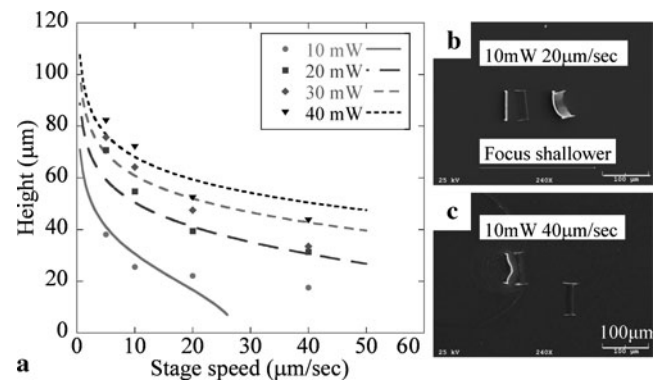
polymerized wall is shown in Fig. 5c. The walls were exposed at a power of 10 mW and a speed of 40 μm/s, giving $P^2/v = 2.5$ mW^2 s/μm, which violates (13). To compare with the under-polymerization, Fig. 5b shows walls exposed at the same power and a speed of 20 mW, giving $P^2/v = 5$ mW^2 s/μm which satisfies (13).

Using (8), we calculated the wall heights corresponding to the measured wall width under the different powers and speeds shown in Fig. 5a. The curves are generated by combining (8) and (10) and substituting in the value of the parameter C'_{th}. The higher-speed region of the curve with circle symbols at $P = 10$ mW indicated under-polymerization of the photoresist, also shown in Fig. 4a.

5 Example structures

5.1 2D flow systems

As a first stage in the development of a system to fabricate 3D microporous structures, we fabricated a single-layer 900 μm × 700 μm maze with a microchannel measuring 100 μm in width and 40 μm in height. The channel vertical sidewall was 5.5 μm wide, as shown in Fig. 6a. The SU-8 maze was fabricated with a pulse energy of 1.6 nJ and a power of 160 mW with a stage scanning speed of 10 μm/s. To achieve a high aspect ratio of height to width, we did not apply the beam expander shown in Fig. 1. The input beam diameter was 3.1 mm and the $1/e^2$ focal spot radius w_0 was 8 μm. The larger focal spot radius results in a larger Raleigh range of 250 μm and a higher height-to-width aspect ratio of 27:1 for the exposed volume. We applied a high pulse energy with an average power of 160 mW and a speed of 10 μm/s to make strong SU-8 walls.

Figures 6a, d, e, and f show several 2D micromodel patterns fabricated for microfluidic studies [41]. Figure 6a

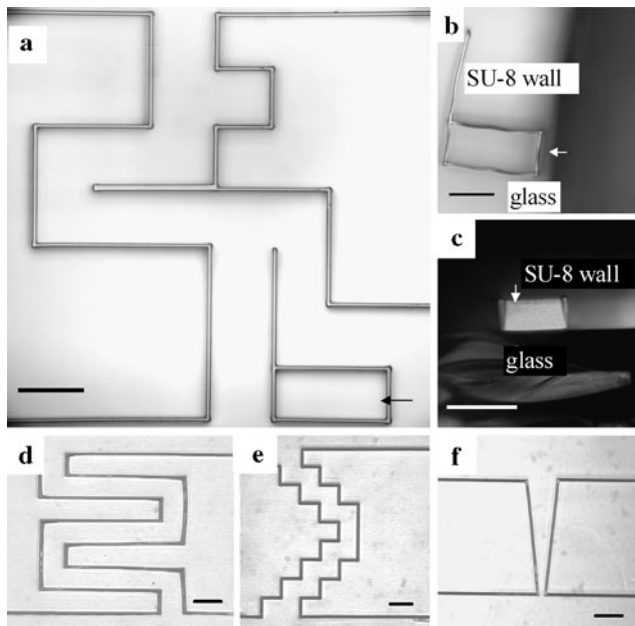**Fig. 6** Optical microscope images of developed SU-8 microchannels exposed at a power of 100 mW and a speed of 10 μm/s without beam expander. The bars in the graph are 100 μm. In **a** the lateral plane image shows clean fabrication and good attachment at the base. In **b** and **c** we mechanically cut the cover slip to image the side view of the wall. The arrows point to the same wall. In **d**, **e**, and **f** are patterns fabricated for various microfluidic purposes

Fig. 7 SEM image of **a** the three-layer pattern with random holes in all layers, unit-cell size 30×30 μm^2, tilted by 30 degree, magnification 600×; **b** the three-layer shifted pattern, unit-cell size 45×45 μm^2, tilted by 30 degree, magnification 600×; **c** the same pattern as in (**a**), tilted by 30 degree, magnification 1k×; **d** the same pattern as that in (**a**) without tilting, magnification 240×; **e** the same pattern as that in (**b**), without tilting, magnification 1k×. The structures are exposed at a power of 10 mW and a speed of 10 μm/s with beam expander

shows an optical image of a micromodel viewed from the top. The wall in the middle of the sample is twice as wide as the others because it was scanned back and forth twice with a separation of 5 μm. Figure 6b and c both show the 'b' shape pattern in Fig. 6a. We cut the sample from the side of the 'b' shape and acquired an image with the optical microscope at a magnification of 20×. The side view image is shown in Fig. 6c, from which the wall height was determined to be 40 μm. The pattern in Fig. 6d and e was fabricated to study the motion of fluid-fluid interfaces around corners and to measure the interfacial area [35–37]. In Fig. 6f, a channel with a linearly decreasing width from 100 μm to 20 μm is shown.

5.2 3D flow systems

3D microporous structures were laser direct-written level-by-level. The channel and fluid ports were exposed by UV broad illumination. The sample thickness was set at 40 μm for flow measurements. The experimental conditions giving the shortest wall, $P = 10$ mW and $v = 10$ μm/s, were chosen. A low pulse energy of 0.1 nJ was used, and the beam expander was used to obtain a smaller height-to-width ratio of 10:1 in order to fit 3 levels into a 40 μm thick SU-8 micromodel. The appropriate exposure was determined from the exposure curves shown in Figs. 4 and 5, which give the relationship between the lateral width of the walls, the pulse en-
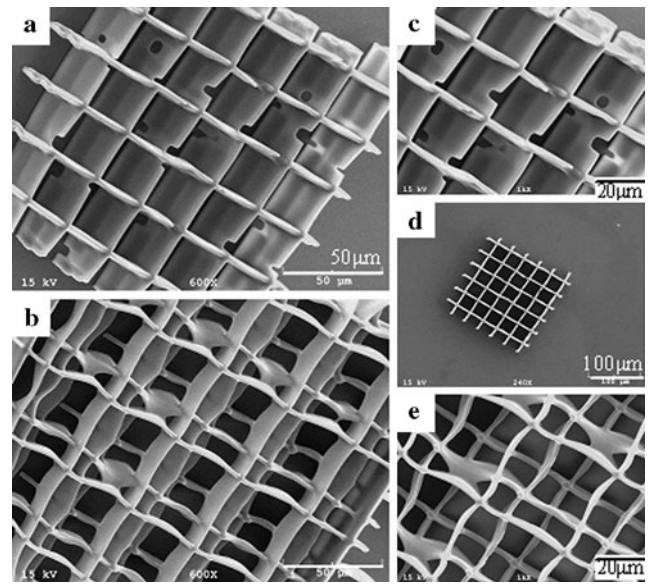
ergy, and the exposure speed. Using a combination of computer simulation and exposure experiments, we controlled the Rayleigh range to be compatible with the microstructure geometry, which is the most important part of 3D microstructure fabrication. The Rayleigh range was 60 μm. The wall width and height were approximately 2 μm and 20 μm respectively at this condition. The overlap between levels was approximately 5 μm and the bottom level was 5 μm beneath the substrate and 15 μm above. Thus, three levels were fit into the 40-μm deep microfluidic structure. Two types of 3-D microstructures, shown in Fig. 7, were fabricated to explore fluid distributions.

The first pattern shown in Fig. 7a is a "chessboard" pattern with walls that contain gaps at random locations in the three levels. We exposed horizontal and vertical walls level-by-level at the same X and Y locations but with 10 μm difference in focal depth in the Z direction. As the laser exposed the wall, the laser beam was blocked to make the gaps. The width of the gap was controlled by the stage speed and beam-block time. The width of the wall is 2.2 μm and the height is about 20 μm for each single wall. The total thickness of the three levels is approximately 40 μm and the overlap between levels is approximately 5 μm. The width of the random gaps in Fig. 7a ranges from 1.6 μm to 7.5 μm.

The second pattern shown in Fig. 7b is a shifted 3-level pattern forming crossing pores that force fluid to move in three dimensions. On each level we exposed a single-level

chessboard pattern with a full size of 45 μm × 45 μm and shifted 15 μm in both X and Y direction and shifted 10 μm in focal depth in the Z direction. The suspended walls in the center level span 45 μm and support the upper-level chessboard pattern. We also fabricated samples with spans of 30 μm and 60 μm. The walls exhibit strains (i.e. "waviness") but the pattern provided adequate mechanical strength for flow measurements. This waviness of the suspended walls was not caused by the vibration of the stage because it was not found in the attached walls under the same experimental conditions.

6 Mechanical instability

6.1 Wall length study

The mechanical distortion of the exposed walls depends on many factors, such as the average exposure power, the stage speed, and the wall dimensions. These factors have complex relationships, e.g. the average power and the stage speed determine the wall width according to the relationship of (9). Therefore, we first studied the dependence on wall length. Furthermore, we developed a method to study the instability by extracting the 1D wall shape from the 2D micrograph to determine the spatial frequency spectrum of different lengths of walls.

To study the relationship between mechanical instability and the wall length, we exposed walls at lengths of 50 μm, 100 μm, 200 μm, 400 μm, and 800 μm. For all lengths we fixed the average exposure power at 10 mW and the stage speed at 10 μm/s, which are the same conditions as for the two 3-D micromodels. Optical and SEM micrographs of the 200 μm long wall are shown in Fig. 8. The horizontal walls were fabricated as the "support" of the vertical suspended walls. The horizontal walls were 40 μm high and exposed at a power of 60 mW and a speed of 10 μm/s without beam expansion. A schematic of the wall structure is shown in Fig. 9a. To provide sufficient support to the suspended walls, a higher average power, 60 mW, was used for the support walls compared with the power for the suspended walls at 10 mW. We exposed the vertical walls as described in the calibration section, with the focal depth becoming shallower from left to right with a difference of 3 μm between steps. The left 4 walls in Fig. 8a and b are attached to the substrate with different heights and the right 4 walls are suspended between the "support" walls as a bridge. Although the 4 walls were suspended at different heights by being exposed at different focal depths, their mechanical instability would be the same because they are suspended regardless of the gap underneath. The 1st left wall in Fig. 9b is directly attached to the substrate and also has waviness. The gap between two support walls determined the wall length and the separation
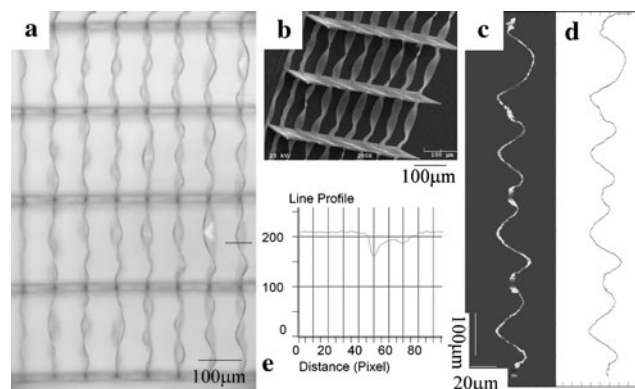

Fig. 8 **a** Optical micrograph of the group with 200 μm wall length exposed at a power of 10 mW and a speed of 10 μm/s with beam expander. The focal depth of the vertical wall is deeper from right to left; **b** the SEM image of the middle area of the walls in (**a**), at a magnification of 200× and tilted at 45°, showing the focal depth changing from the connection part of the "skeleton" wall and the "bridge" wall; **c** the intensity profile of the line in (**a**); **d** the 1st right wall in (**a**) with the background removed; and **e** the extracted 1D wall curve of the 1st right wall in (**a**)
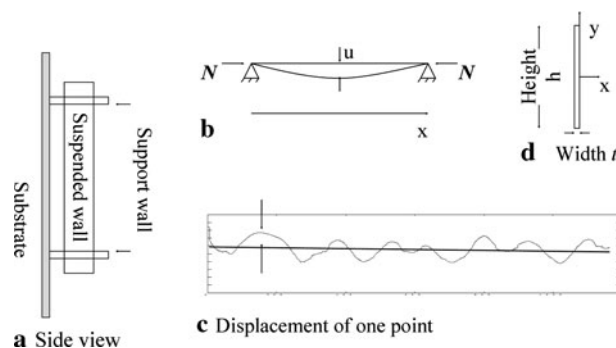

Fig. 9 **a** Schematic of the side view of the wall structure design; **b** schematic of a beam with axial loading N; **c** the algorithm to calculate the displacement; the *curve* shows extracted wall data fit by a straight line. **d** the axial cross section of a photoresist wall

between two bridge walls was fixed at 70 μm, which is far enough to prevent interaction between two walls.

After taking the optical images of the exposed walls, the 1D wall shape was extracted from the 2D image. First, the average value of all the pixels in the image was taken as the background value. The pixels were set to the background if their values were within 10% of the average value. Figure 8c shows an example of the wall with the background removed. To find the 1D shape from the 2D image, the wall position was extracted from each horizontal line in Fig. 8c. For each line, the pixel on the walls had a lower value than the background (Fig. 8e). Thus a threshold value was set at 80% of the minimum value plus 20% of the background value. The wall position was determined by averaging the positions of points lower than the threshold value. An example of the extracted wall curve is shown in Fig. 8d. To optimize the data extraction process, images were focused on each wall sepa-

rately. For example, Fig. 8a was an image focused on the 1st right wall.

The equation for analysis of the distortion is derived by considering a beam subjected to an axial compressive force N [42], shown in Fig. 9b.

$$EI\frac{d^2u}{dx} + Nu = 0 \qquad (14)$$

where x is the longitudinal coordinate along the beam, u is the axial displacement perpendicular to the beam, E is Young's Modulus, and $I = \frac{1}{12}ht^3$ is its moment. The solution of (14) is a harmonic series

$$u = A_1 \sin\frac{\pi x}{L} + A_2 \sin\frac{2\pi x}{L} + A_3 \sin\frac{3\pi x}{L} + \cdots \qquad (15)$$

where L is the beam length and A_i ($i = 1, 2, 3, \ldots$) is an amplitude parameter. The corresponding spatial frequencies are $1/2L$, $1/L$, and $3/2L$. A Fourier transform was applied to the extracted wall data to determine the spatial frequency of the instability. The analysis was performed 4 times for each wall length based on 4 different suspended walls at each length. From the average spectra we recorded the amplitude and the frequency of the largest Fourier component for each wall length. To reduce the random error introduced by the exposure, baking, developing, and rinsing procedures, we repeated the experiment 4 times under the same conditions. For each group, we plotted the spatial frequency and the spectral amplitude in terms of the wall length, based on the values of the main frecuency components. Finally, we averaged the 4 groups of data, and the results are plotted in Fig. 10. The error bars in the figure are the standard deviation from the 4 sets of data. The amplitude increases rapidly initially and then saturates as the wall length increases. Similarly, the spatial frequency drops sharply as the wall length increases from 50 μm to 200 μm, and then becomes nearly constant for longer walls.

In beam mechanics, the critical loading N_{er} for wall buckling is

$$N_{er} = \frac{\pi^2}{3}Eht^3f^2 = \frac{\pi^2}{3}EAt^2f^2 \qquad (16)$$

where f is spatial frequency, E is the Young's Modulus of SU-8, which is 4.02 GPa at room temperature, h is the height and t is the thickness of the wall. At room temperature, the critical force is $N_{er} = 0.21$ mN. Because the deformation of the photoresist wall was observed to become independent of the wall length for longer walls, we consider the force F of thermal expansion as a possible force source

$$F = EA\frac{\Delta L}{L} \qquad (17)$$

where, A is the wall cross section area, and L is the photoresist wall length. The temperature increases to 95°C during the post-exposure bake for a change in temperature of approximately 70°C. The length difference between the photoresist and the glass substrate upon heating is

$$\Delta L = (\alpha_{SU\text{-}8} - \alpha_{glass})L\Delta T \qquad (18)$$

where α is the coefficient of thermal expansion. Substituting ΔL in (17) by (18), gives

$$F = EA(\alpha_{SU\text{-}8} - \alpha_{glass})\Delta T \qquad (19)$$

which shows the independence of the force F on the wall length L. The coefficients of thermal expansion are $\alpha_{SU\text{-}8} = 5 \times 10^{-5}$ K^{-1} and $\alpha_{glass} = 7 \times 10^{-6}$ K^{-1}. This gives a calculated force of $F = 0.48$ mN. This exceeds the critical force of $N_{er} = 0.21$ mN from (16) at room temperature, and the critical force is expected to be even lower at the elevated bake temperatures.

An important observation we have made after cooling down to room temperature, but before development, is a surface relief associated with the polymerized section. This surface relief after the bake shows the deformation. Therefore, the deformation is clearly caused by the bake process, and not by the release of the structure by development. The likely source of the mechanical distortion is the differential expansion between the photoresist and the glass substrate during heating. The walls and surrounding unexposed photoresist are under compressive strain causing the deformation as the walls polymerize at the elevated temperature. The deformation is retained even after cooling back to room temperature. To mitigate this effect, it may be necessary to use lower post-bake temperatures and to use slower heating rates. It might also be possible to match the thermal expansion of the photoresist with other substrates. This would enable free-standing broad-area structures to be fabricated free of deformations.

6.2 Wall-width study

To study the instability as a function of the wall width, we varied the width and excluded other factors such as the wall height. The width is determined by the exposure dosage and related to the beam power and the stage speed. It is difficult to vary only the width without any height change because the width-to-height ratio is determined by the focal spot radius. Therefore, we fabricated double wall experiments. We kept the exposure dosage and focal spot radius the same as for the previous length study with a power of 10 mW, a speed of 10 μm/s, and a focal spot radius of 4 μm. We exposed a single wall, as in the previous experiments, and then exposed another wall parallel to the 1st wall with the stage moved by 2 μm. After crosslinking, these two walls formed one double wall. The width of a double walls was approximately twice that of a single wall width, because the distance between the
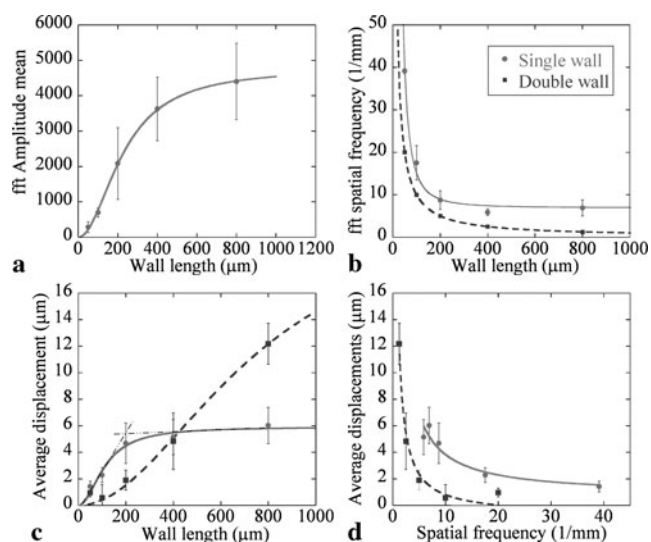
Fig. 10 Fourier amplitudes and frequencies for single and double walls. The data points are the mean value of 4 independent groups of experiments. The error bar is the standard deviation of the 4 data sets. The spectral amplitude (**a**), the spatial frequency (**b**), and the average displacement (**c**) as a function of the wall length, and the average displacement (**d**) as a function of the spatial frequency. The *solid* and *dashed lines* show the data of the single and the double walls, respectively
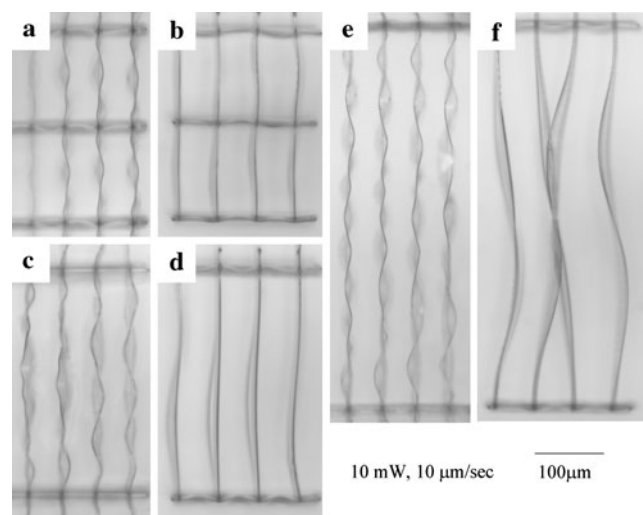

Fig. 11 The comparative optical images of the single (**a**, **c**, **e**) and double (**b**, **d**, **f**) walls at a wall length of 200 μm (**a**, **b**), 400 μm (**c**, **d**), and 800 μm (**e**, **f**). All walls are suspended. The intervals between the single walls are 70 μm and those between the double walls are 80 μm. The differences of instability between the single and double walls are obvious, with higher spatial frequency for the single walls than for the double walls

two walls is 2 μm, which is approximately the width of a single wall. In this case, the height of the suspended wall remained approximately the same. Thus, we only varied the wall width while keeping other factors fixed.

To study the dependence on the wall width, we repeated the same experiments for the double wall as in Sect. 6.1. The comparative optical images between the single and double walls at the lengths of 200 μm, 400 μm, and 800 μm are shown in Fig. 11. Compared to the single walls, the double walls have much lower spatial frequency and larger displacements.

Data analysis was repeated as for the previous section, but no frequency peaks were present in the spectra. Therefore, a different algorithm was used to measure the waviness of the wall shown in Fig. 9c. First, the wall profile was extracted through the same method as in Sect. 6.1. A straight line was fit to the wall and the mean value of the displacements between the corresponding points on the wall and on the line was calculated. This average displacement shows how much the wall deviates from a straight line. The calculated average displacements of the single and double wall in Sect. 6.1 are shown in Fig. 10c. The turning point of the single wall from Fig. 10c was around 200 μm, but that of the double wall could not be determined from the graph. Because the displacement increased with the reduction of the spatial frequency, these two variables may be related. Therefore, we defined the spatial frequency of the double wall as $1/L$ (wall length) as observed from the optical images and the average displacement as a function of the frequency, shown in Fig. 10d.

7 Conclusion

In conclusion, we employed two-photon polymerization (2PP) to fabricate large-format 3D microfluidic structures in the epoxy-based photoresist SU-8. The localization and small features of the 2PP exposure in the resist make 3D microstructure fabrication possible. The direct-writing laser machining speeds can produce reasonable large-format-structure fabrication times on the order of 50 minutes for 450 μm × 450 μm. A variety of 2D and two types of 3D microfluidic structures were fabricated by employing the 2PP laser direct-writing method.

The two 3D structures were made by exposing walls under an average power of 10 mW and a stage speed of 10 μm/s. The appropriate exposure was determined by using different average-energy pulses and stage speeds to produce the exposure curve. This gives the relationship between the lateral width of the walls relative to the pulse energy and exposure speed. One 3D structure had gaps with variable sizes located randomly in three levels in the wall. The other structure was a shifted 3-level pattern that would force fluid to move in three dimensions.

Microstructures fabricated by 2PP laser machining that had suspended walls exhibited deformations with distinct Fourier frequencies. Suspended walls with different lengths

and widths were exposed, and the shapes of the walls were extracted to perform an instability study. A simple mechanical analysis of beam buckling indicates that thermal forces exceed the critical loading, caused by differential thermal expansion between the SU-8 and the glass substrate. The subsequent force is independent of the length of the wall and is proportional to the cube of the wall thickness for a fixed wall height.

References

1. P. Yon-Han, P.M. Rentzepis, Appl. Phys. Lett. **6**, 93–95 (1965)
2. D.A. Parthenopoulos, P.M. Rentzepis, Science **245**, 843–845 (1989)
3. J.H. Strickler, W.W. Webb, Opt. Lett. **16**, 1780–1782 (1991)
4. K. Kaneko, H.B. Sun, X.M. Duan, S. Kawata, Appl. Phys. Lett. **83**, 2091–2093 (2003)
5. J. Serbin, A. Ovsianikov, B. Chichkov, Opt. Express **12**, 5221–5228 (2004)
6. V. Ramanan, E. Nelson, A. Brzezinski, P.V. Braun, P. Wiltzius, Appl. Phys. Lett. **92**, 173304 (2008)
7. S. Maruo, O. Nakamura, S. Kawata, Opt. Lett. **22**, 132–134 (1997)
8. H.-B. Sun, T. Kawakami, Y. Xu, J.-Y. Ye, S. Matuso, H. Misawa, M. Miwa, R. Kaneko, Opt. Lett. **25**, 1110–1112 (2000)
9. P. Galajda, P. Ormos, Appl. Phys. Lett. **78**, 249–251 (2001)
10. S. Kawata, S. Hong-Bo, Appl. Surf. Sci. **208–209**, 153–158 (2003)
11. R. Guo, S.Z. Xiao, X.M. Zhai, J.W. Li, A.D. Xia, W.H. Huang, Opt. Express **14**, 810–816 (2006)
12. T.W. Lim, S.H. Park, D.Y. Yang, H.J. Kong, K.S. Lee, Appl. Phys. A **84**, 379–383 (2006)
13. M.P. Joshi, H.E. Pudavar, J. Swiatkiewicz, P.N. Prasad, B.A. Reianhardt, Appl. Phys. Lett. **74**, 170–172 (1999)
14. S. Klein, A. Barsella, G. Taupier, V. Stortz, A. Fort, K.D. Dorkenoo, Appl. Surf. Sci. **252**, 4919–4922 (2006)
15. S. Kawata, H.B. Sun, T. Tanaka, K. Takada, Nature **412**, 697–698 (2001)
16. K.S. Lee, R.H. Kim, P. Prabhakaran, J. Nonlinear Opt. Phys. Mater. **16**, 59–73 (2007)
17. W. Haske, V.W. Chen, J.M. Hales, W.T. Dong, S. Barlow, S.R. Marder, J.W. Perry, Opt. Express **15**, 3426–3436 (2007)
18. F. Formanek, N. Takeyasu, T. Tanaka, K. Chiyoda, A. Ishikawa, S. Kawata, Opt. Express **14**, 800–809 (2006)
19. T.W. Lim, Y. Son, D.Y. Yang, H.J. Kong, K.S. Lee, S.H. Park, Appl. Phys. A **92**, 541–545 (2008)
20. W. Linhart, F. Peters, W. Lehmann, K. Schwarz, A.F. Schilling, M. Amling, J.M. Rueger, M. Epple, J. Biomed. Mater. Res. **54**, 162–171 (2001)
21. B.B. Lakshmi, C.J. Patrissi, C.R. Martin, Chem. Mat. **9**, 2544–2550 (1997)
22. S.C. Jose, M.A. Rahman, O.A. Cirpka, Water Resour. Res. **40**, 13 (2004)
23. N.D. Lai, W.P. Liang, J.H. Lin, C.C. Hsu, C.H. Lin, Opt. Express **13**, 9605–9611 (2005)
24. N.C. LaBianca, J.D. Gelorme, in *Advances in Resist Technology and Processing XII* (SPIE, Santa Clara, 1995), p. 846
25. R. Feng, R.J. Farris, J. Micromech. Microeng. **13**, 80–88 (2003)
26. J.M. Shaw, J.D. Gelorme, IBM J. Res. Dev. **41**, 81 (1997)
27. C.H. Lee, T.W. Chang, K.L. Lee, J.Y. Lin, J. Wang, Appl. Phys. A **79**, 2027–2031 (2004)
28. K.Y. Lee, N. LaBianca, S.A. Rishton, S. Zolgharnain, J.D. Gelorme, J. Shaw, T.H.P. Chang, J. Vac. Sci. Technol. B **13**, 3012–3016 (1995)
29. W.H. Teh, U. Durig, U. Drechsler, C.G. Smith, H.J. Guntherodt, J. Appl. Phys. **97**, 54907–54901 (2005)
30. H. Lorenz, M. Despont, N. Fahrni, N. LaBianca, P. Renaud, P. Vettiger, J. Micromech. Microeng. **7**, 121–124 (1997)
31. X.B. Yin, N. Fang, X. Zhang, I.B. Martini, B.J. Schwartz, Appl. Phys. Lett. **81**, 3663–3665 (2002)
32. M. Gaudet, J.-C. Camart, L. Buchaillot, S. Arscott, Appl. Phys. Lett. **88**, 024107 (2006)
33. T. Kondo, K. Yamasaki, S. Juodkazis, S. Matsuo, V. Mizeikis, H. Misawa, in *Three-Dimensional Microfabrication by Femtosecond Pulses in Dielectrics* (Elsevier, Strasbourg, 2004), pp. 550–556
34. S. Hong-Bo, S. Kawata, J. Lightwave Technol. **21**, 624–633 (2003)
35. J.T. Cheng, L.J. Pyrak-Nolte, D.D. Nolte, N.J. Giordano, Geophys. Res. Lett. **31** (2004)
36. D.Q. Chen, L.J. Pyrak-Nolte, J. Griffin, N.J. Giordano, Water Resour. Res. **43** (2007)
37. L.J. Pyrak-Nolte, D.D. Nolte, D.Q. Chen, N.J. Giordano, Water Resour. Res. **44** (2008)
38. V.J. Niasar, S.M. Hassanizadeh, L.J. Pyrak-Nolte, C. Berentsen, Water Resour. Res. **45** (2009)
39. J. Serbin, A. Egbert, A. Ostendorf, B.N. Chichkov, R. Houbertz, G. Domann, J. Schulz, C. Cronauer, L. Frohlich, M. Popall, Opt. Lett. **28**, 301–303 (2003)
40. S. Juodkazis, V. Mizeikis, K.K. Seet, M. Miwa, H. Misawa, Nanotechnology **16**, 846–849 (2005)
41. L. Yihong, L.J. Pyrak-Nolte, D. Nolte, in *Toward 3D Microfluidic Structures Fabricated with Two-Photon Laser Machining* (IEEE, Baltimore, 2007), pp. 2261–2262
42. S.P. Timoshenko, J.M. Gere, *Theory of Elastic Stability* (McGraw-Hill, New York, 1961)